Proceedings 10th NUMGE 2023
10th European Conference on Numerical Methods in Geotechnical Engineering
Zdravkovic L, Kontoe S, Taborda DMG, Tsiampousi A (eds)

https://doi.org/10.53243/NUMGE2023-353

A DEM based micromechanical study on influence of lateral boundaries on instability response of sand under biaxial shearing

M.S. Negi[1], M. Mukherjee[1]

[1]*School of Civil and Environmental Engineering, Indian Institute of Technology Mandi, India*

ABSTRACT: DEM based numerical studies have shown that the formation of instabilities in granular materials is a continuous process and is influenced by both internal inhomogeneity and imposed stress states. Present study explores the influence of two types of lateral boundary conditions, stress controlled flexible boundary and velocity controlled rigid boundary, on the mechanical behaviour and instability response of sand under biaxial shearing employing DEM. It is observed that the specimen with flexible boundary estimates higher deviator stress as compared to that of rigid boundary, which is attributed to the additional confinement induced by the flexible boundaries. Further, for dense specimens with flexible boundaries, bulging type deformation is noticed accompanied with shear bands; whereas, for rigid lateral boundaries, the specimen always retains the initial outer shape enforcing the particles to adapt the kinematics of the wall boundary. For loose specimens, diffused instability mode is observed with surficial bulging only for flexible boundaries. The instability responses are assessed with the help of microlevel interaction at particle scale and evolution of meso-structure.

Keywords: Biaxial text; Flexible boundary; Rigid boundary; Instability

1 INTRODUCTION

Instabilities in geomaterials often act as an indicator towards failure of geo-structures (Widuliński et al., 2011) and play a key role on the occurrence of landslides, liquefaction, and debris flows. In a boundary value problem, the onset of such instabilities is associated with transition from an initial homogeneous deformation field to a nonhomogeneous one. Similar to the geotechnical field scenarios, signatures of instabilities are also encountered in the laboratory element level tests while assessing the constitutive response of the geomaterials. Owing to the resemblance of stress-strain states with the plane strain condition, which is conformed by majority of the geotechnical structures, biaxial tests are often employed for laboratory characterisation of the instability onset and its subsequent impact on the overall material response (Andrade and Borja, 2007; Han and Drescher, 1993). These instabilities detected at the macrolevel initiate at the microlevel and, with continued deformation, spread across the entire assembly affecting the constitutive response of the particulate assembly. Therefore, particle-based analysis, such as discrete element method (DEM), can be extremely helpful in comprehending the micromechanics of instabilities in geomaterials.

DEM based numerical studies have shown that the formation of instabilities in granular materials is influenced by both internal inhomogeneities and imposed boundary conditions (Gu et al., 2014; Lü et al., 2019; Tian et al., 2020). Two types of lateral boundaries, i.e. displacement controlled rigid and stress controlled flexible boundaries, are commonly adopted for the simulation of any element level test in DEM. Rigid lateral boundary is widely employed in DEM simulations due to the ease of applying the desired stress state by the servomechanism (Mohammad et al., 2018; Tian and Liu, 2018). However, in this case, the boundary walls have a tendency to inhibit the deformation of the specimen and may restrict the development of shear band (Cheung and O'Sullivan, 2008). On the contrary, the flexible lateral boundary is usually modeled by a separate set of bonded particles, which allows the tensile force to develop at the particle contacts mimicking the membrane flexibility. The required stresses on the flexible lateral boundary are usually achieved by applying equivalent forces to these membrane particles directly (Wang and Leung, 2008). In specimens with flexible lateral boundaries, the shear band can develop naturally since the particles near the lateral boundaries are not restrained kinematically (Cheung and O'Sullivan, 2008; Cil and Alshibli, 2014; Tian et al., 2020). Since both these types of lateral boundaries are widely used nowadays to assess the constitutive response from the single element test simulations, it is crucial to comprehend how these lateral boundaries affect the instability onset and subsequent shearing behavior of granular assembly.

DEM simulations have been carried out in the present work incorporating both flexible and rigid lateral boundaries and the influence of these boundaries on the instability response of dense and loose sand has been investigated under biaxial shearing. In this regard, the nucleation and manifestation of localized and diffused instability modes have been analyzed from the micro-level attributes like spatial variation of porosity, particle relative displacement and particle rotation.

2 BIAXIAL TEST SIMLATION

Drained biaxial test simulations have been conducted using commercially available DEM software, Particle Flow Code-2D, PFC2D (Itasca, 2014). The details of specimen geometry and material parameters are given in Table 1. A linear elastic type contact model with Coulomb friction law has been implemented for representing the normal and shear interaction between the particles. Figure 1 shows the particle size distribution for the sand specimen, which is composed of circular particles of mean particle diameter d_{50} = 0.993 mm.

The biaxial test simulations have been performed in three stages, namely, particle generation, isotropic compression and biaxial shearing stage. For the particle generation phase, a multilayer undercompaction method (UCM) has been adopted (Jiang et al., 2003), where the specimen has been generated in four layers with an initial undercompaction of 5 % in the bottom most layer. This enables to avoid excessive densification of the lower layers owing to the energy transfer between successive layers during the compaction process. In the subsequent isotropic compression phase, the boundary walls are moved inward until the required confining pressure of 300 kPa has been achieved. During this phase, an interparticle friction magnitude of 0 and 1 has been employed in order to generate dense and loose specimens, respectively.

Finally, in the biaxial shearing stage, the interparticle friction value has been restored to its representative value and the specimens are compressed vertically with the strain-controlled top and bottom platen at a constant velocity of 0.05 m/s. With this rate, the inertia number of the specimen has been found to be much smaller than 10^{-3}, i.e., the sample remained in the quasi-static regime throughout the test (Midi, 2004). During the shearing stage, the confining pressure of 300 kPa has been maintained on the specimen using either a velocity-controlled rigid boundary or a stress-controlled flexible lateral boundary. Figure 2 depicts the schematic diagram of the biaxial test configuration along with the two types of modeled lateral boundaries. The flexible membrane has been modeled with a string of uniform sized small circular particles placed adjacent to the periphery of the specimen. After placement, the membrane particles are linked together by the built-in linear contact bond model of PFC2D (Itasca, 2014). Additionally, equivalent normal forces are applied directly over the membrane segments in order to achieve the target confining pressure on the specimen boundary (Wang and Leung, 2008). On the contrary, the rigid lateral boundaries have been modeled by frictionless rigid walls. In such cases, the confining pressure on the specimen boundary has been achieved through a velocity-controlled servo mechanism by moving the side walls inward or outward based on the requirement.

The pre-shearing porosities of the dense and loose specimens with flexible and rigid lateral boundaries have been listed in Table 2 along with the corresponding abbreviations. All the specimens have been sheared until an axial strain level of 35 %. The macro and micro level responses of these specimens during biaxial shearing have been discussed in the subsequent sections.

Table 1. Model geometry and material parameters used for the DEM simulation

Parameter	Value	Unit
Soil specimen property		
Initial specimen height	100	mm
Initial specimen width	50	mm
Number of particles	6700	
Particle properties		
Density	2650	kg/m^3
Particle friction	0.5	-
Normal contact stiffness	1.5×10^8	N/m
Tangential contact stiffness	1×10^8	N/m
Flexible membrane properties		
Density	1800	kg/m^3
Particle radius	0.01	mm
Normal bond strength	1×10^{300}	Pa
Shear bond strength	1.5×10^{300}	Pa
Normal contact stiffness	1×10^7	N/m
Shear contact stiffness	1×10^7	N/m
Rigid wall properties		
Wall friction	0.0	-
Normal contact stiffness	1.5×10^8	N/m
Tangential contact stiffness	1×10^8	N/m

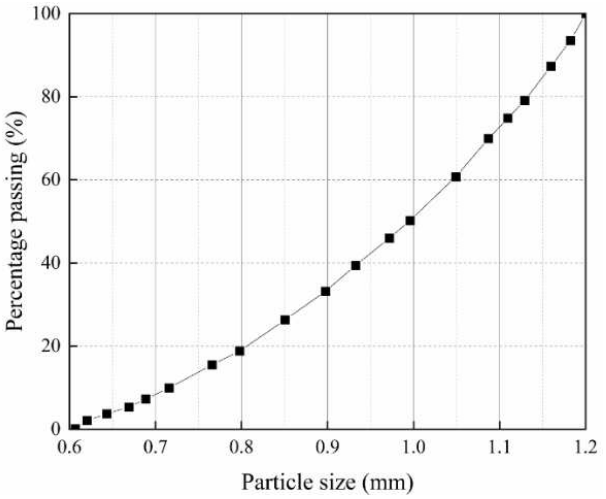

Figure 1. Particle size distribution

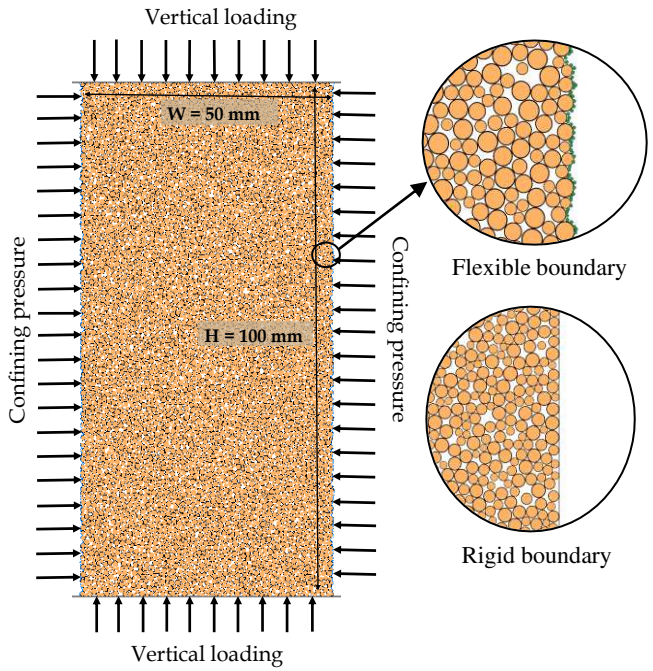

Figure 2. Schematic diagram of the biaxial test configuration along with the two types of modeled boundaries

Table 2. Summary of the biaxial test simulations

Lateral boundary	Density state	Pre-shearing porosity	Abbreviation
Flexible	Dense	0.1601	FD
Flexible	Loose	0.1929	FL
Rigid	Dense	0.1602	RD
Rigid	Loose	0.1931	RL

3 EFFECT OF LATERAL BOUNDARIES ON THE MACRO LEVEL RESPONSE

Stress-strain and volumetric characteristics have been used to assess the macro level mechanical responses. An estimate of these field variables has been made based on the average value of three overlapped area elements (measurement circles) that are placed within the specimens (Tian et al., 2020). In order to obtain better estimates of stress and strain fields, these measurement circles have been considered to evolve as the deformation process continues, maintaining a constant area coverage (95% of total specimen area) governed by the deformed specimen configuration (Negi and Mukherjee, 2022).

Figure 3 depicts the stress-strain and volumetric response of the dense and loose specimens with flexible and rigid lateral boundaries. In both the dense specimens (FD and RD), the stress deviator ($\sigma_d = \sigma_1 - \sigma_2$) attains a peak at 2 % axial strain, followed by a softening response reaching to residual stress level at large strain. Similarly, the volumetric response first exhibits a compressive response up to 0.6 % axial strain, followed by a dilative response with increasing axial strain (Figure 3(b)). On the contrary, loose specimens with both flexible and rigid boundaries (FL and RL) exhibit a hardening type stress-strain response that reaches an asymptotic value around the axial strain level of 12 % (Figure 3(a)). With continued shearing, an overall compressive type volumetric response can be observed for these loose specimens. It is interesting to note that both the dense and loose specimens with flexible lateral boundaries (FD and FL) exhibit higher shear stresses up to 5 % axial strain level as compared to the corresponding specimens with rigid lateral boundaries (RD and RL). This stress enhancement is also accompanied by an enhanced volumetric compression in the specimens with flexible lateral boundaries (Figure 3(b)). This enhancement of stresses and volumetric compression is attributed to the additional confining pressure, which is exerted by the lateral membrane in order to support the radially expanding specimen under shearing. Further, this additional confining pressure is governed by the membrane stiffness (Li et al., 2022). The inset of Figure 3(a) depicts the additional confinement, i.e., confining pressure in addition to the applied confinement of 300 kPa, which is exerted upon the specimens. It can be noticed that both the dense and loose specimens with flexible lateral boundary experience additional confinement of around 10 kPa. For the case of specimens with servo-controlled rigid lateral boundaries, the magnitude of such additional confining pressure is less than 5 kPa.

It is to be noted that localized instability in the form of cross type shear bands appears in dense specimens subjected to both types of boundaries. On the contrary, diffused instability mode with surficial bulging is observed only for the loose specimens with flexible boundaries. The localised and diffused instability within the dense and loose specimens have been discussed in detail in the subsequent section.

4 INFLUENCE OF LATERAL BOUNDARIES ON THE INSTABILITY RESPONSE

The effect of lateral boundaries on the instability response of dense and loose specimens has been analyzed in this section based on the micro and meso level changes at the particle scale. In this regard, the microstructure of the specimen has been investigated by local variation of porosity, relative particle displacement, and rotation fields within the specimen.

4.1 Dense specimens

In the present study, irrespective of the boundary types, dense specimen exhibits localised instability in the form of two conjugate persistent shear bands. In such localized shear bands, porosity is usually greater than the average porosity of the specimen (Alshibli et al., 2003; Gu et al., 2014; Lü et al., 2019). Hence, a local density variation within the specimen has been analyzed here through the spatial variation of porosity. The relative displacements between the particles have also been found to be an effective way to identify the initiation

and subsequent evolution of localised instability (Druckrey and Alshibli, 2017; Lü et al., 2019). In this regard, the relative displacement (RD) for any particles in the specimen has been calculated as

$$RD = \frac{1}{n}\sum_{i=1}^{n} rd_i \quad (1)$$

$$rd_i = norm\,(\delta - \delta_i) \quad (2)$$

where n is the total number of particles in contact with the target particle, rd_i is the magnitude of relative displacement for a single contacting particle, δ and δ_i are the displacement vectors of the target particle and the i^{th} neighboring particle in contact, respectively.

In addition to porosity and particle relative displacement, the accumulated particle rotations, i.e., the cumulative rotation of the particles noted from the beginning of the shearing, has also been considered for analysing the localized instability within the specimen. The shear band locations within the specimen are usually associated with very high particle rotations (Jiang et al., 2010). Figure 4 depicts the spatial variation of the porosity, particle relative displacement and particle rotation at 35 % strain level for both the dense and loose specimens subjected to flexible and rigid lateral boundaries. It can be observed that both the dense specimens form cross type shear bands with large volumetric dilation, relative particle displacement and particle rotation within the bands. Further, it is also evident from Figures 4(b, d, f, h, j, and l) that the specimen with rigid lateral boundary always retains its original rectangular shape as the particles within such specimen are forced to adapt to the kinematics of the boundary walls. For such boundaries, a uniform lateral deformation is imposed externally through the inward/outward movement of the lateral wall. This causes an equal magnitude of inward/outward displacement for all the boundary particles along the wall height and thus the specimen maintains its original rectangular shape throughout the deformation process. However, this is not the case with flexible lateral boundaries, which provide less restraint to the particles for their movement in the lateral direction. This further leads to the irregular deformed shape of the specimen when subjected to the flexible lateral boundaries.

In addition to the onset strain, the other attributes of the shear band, such as thickness and inclination, can be obtained from the spatial variation of different field quantities like porosity (Gu et al., 2014; Jiang et al., 2010; Lü et al., 2019), relative displacement (Druckrey and Alshibli, 2017; Lü et al., 2019) and particle rotations (Jiang et al., 2010). In the present study, the inclination of the shear band has been calculated at 35 % axial strain level, i.e., the strain level where fully developed persistent shear bands have been noticed. Considering the cross-type nature of the shear band, both left and right bands have been used to calculate the shear band inclination, and the average of these two values has been reported as the final inclination. For this purpose, the band inclination angles are measured from the minor principal stress direction. The onset of localised instability and the thickness of the shear band have been noticed to be almost similar for both the types of lateral boundaries, and hence, not presented here.

The shear band inclination angles, estimated from particle rotation, relative displacement, and porosity field, have been depicted in Figure 5 at 35 % axial strain level for dense specimens with flexible and rigid lateral boundaries. It is evident that the specimen with rigid lateral boundaries exhibits higher shear band inclination as compared to the specimen with flexible lateral boundaries. This is attributed to the constrained motion of the particles inside the specimen for the latter case, which leads to a cross-type shear band forming from one corner of the boundary to another diagonally opposite corner of the specimen. However, in case of the specimen with flexible lateral boundaries, particles are able to move and rotate freely in the lateral direction resulting in an irregular deformed shape and hence, the band inclination is lesser as compared to the rigid lateral boundary case.

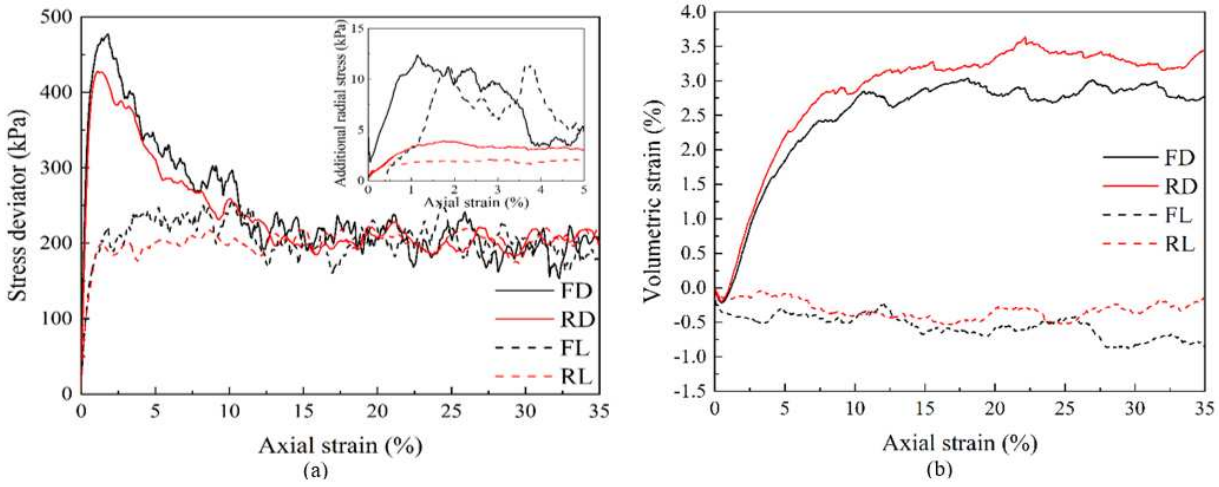

Figure 3. (a) Stress-strain and (b) volumetric response of the dense and loose specimens under biaxial shearing. Inset in Figure 3(a) shows the evolution of additional radial stress exerted by lateral boundaries

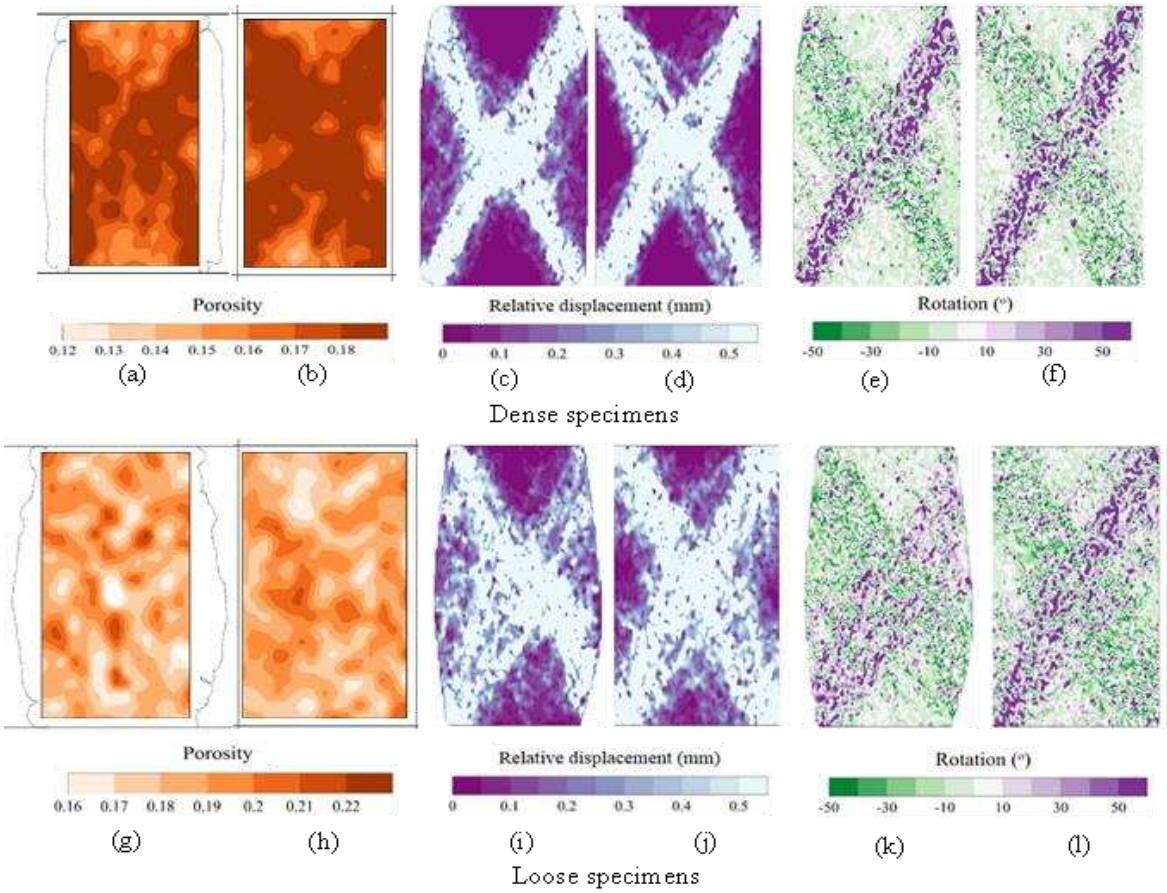

Figure 4. (a, b and g, h) Porosity, (c, d and i, j) relative particle displacement, and (e, f and k, l) particle rotation contours for the dense and loose specimens during biaxial shearing at 35 % axial strain level with flexible and rigid lateral boundaries, respectively

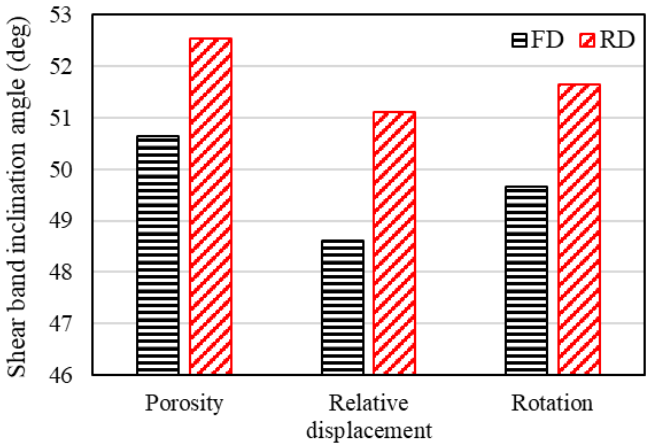

Figure 5. Shear band inclination angle estimated from particle rotation, relative displacement, and porosity field at 35 % axial strain level for dense specimens with flexible and rigid lateral boundaries

4.2 Loose specimens

It can be observed from Figures 4(g-l) that the loose specimens with both types of boundaries exhibit diffused type instability which is accompanied with large relative particle displacement and particle rotation spread across the whole specimen. For both these cases, an indistinct and disorganized cross-type region of large relative displacement and rotation is evident within the specimen. Unlike the case of localized shear bands with high porosity as noticed in the dense specimen, the porosity field in loose specimen depicts multiple pockets of high and low porosity regions spread across the complete specimen. Since the particles can move and rotate freely in the lateral direction for the specimen with flexible lateral boundaries, significant surficial bulge formation can be noticed along the specimen surface (Figures 4(g, i and k)). Interestingly, such surficial bulging is absent from the specimen with rigid lateral boundary due to the imposed kinematic constrained at the lateral boundaries. Hence, it can be inferred that not only the localized instability, consideration of flexible lateral boundary also enables unconstrained formation of diffused instability while simulating biaxial shearing of granular soil.

5 CONCLUSIONS

In the present work, two different types of lateral boundaries, i.e., rigid and flexible boundaries, commonly adopted in DEM simulations have been analysed focusing on their effects towards the instability response of sand under biaxial shearing. It has been found that the specimen with flexible boundaries exhibits higher deviator stress and more volumetric compression due to the

additional confinement imposed by the flexible boundaries. Dense specimen with rigid lateral boundaries forms shear bands that originate from one corner of the boundary to another diagonally opposite corner with high band inclination in comparison to the specimen with flexible lateral boundaries. Loose specimens with both types of boundaries exhibit diffused instability accompanied by large particle relative displacements and rotations spread across the whole specimen. However, only in case of the flexible lateral boundaries such diffused instability modes are associated with distinct surficial bulge formation. This surficial bulging is absent from the specimen with rigid lateral boundary due to the imposed kinematic constraint at such boundaries.

6 ACKNOWLEDGEMENTS

The authors would like to acknowledge Dr. Arghya Das from Indian Institute of Technology Kanpur, India for providing access to the PFC 2D software.

7 REFERENCES

Alshibli, K.A., M., Batiste, S.N., Sture, S. 2003. Strain Localization in Sand: Plane Strain versus Triaxial Compression, *Journal of Geotechnical and Geoenvironmental Engineering* **129**, 483–494.

Andrade, J.E., Borja, R.I. 2007. Modeling deformation banding in dense and loose fluid-saturated sands, *Finite Elements in Analysis and Design* **43**, 361–383.

Cheung, G., O'Sullivan, C. 2008. Effective simulation of flexible lateral boundaries in two and three-dimensional DEM simulations, *Particuology* **6**, 483–500.

Cil, M.B., Alshibli, K.A. 2014. 3D analysis of kinematic behavior of granular materials in triaxial testing using DEM with flexible membrane boundary, *Acta Geotechnica* **9**, 287–298.

Druckrey, A. M., Alshibli, K.A. 2017. 3D particle-scale displacement gradient to uncover the onset of shear bands in sand, in: Int. Workshop on Bifurcation and Degradation in Geomaterials. 39–45.

Gu, X., Huang, M., Qian, J. 2014. Discrete element modeling of shear band in granular materials, Theoretical and Applied Fracture Mechanics **72**, 37–49.

Han, C., Drescher, A. 1993. Shear bands in biaxial tests on dry coarse sand. Soils and Foundations **33**, 118–132.

Itasca Consulting Group, Inc. 2014, PFC-Particle Flow Code, Ver. 5.0. Minneapolis.

Jiang, M., Zhu, H., Li, X. 2010. Strain localization analyses of idealized sands in biaxial tests by distinct element method. *Frontiers of Architecture and Civil Engineering in China* **4**, 208–222.

Jiang, M.J., Konrad, J.M., Leroueil, S. 2003. An efficient technique for generating homogeneous specimens for DEM studies. *Computers and Geotechnics* **30**, 579–597.

Li, Z., Kang, J., Li, J., Tai, P., Zhou, Z. 2022. Modeling of flexible membrane boundary using discrete element method for drained / undrained triaxial test. *Computers and Geotechnics* **145**, 104687.

Lü, X., Zeng, S., Li, L., Qian, J., Huang, M. 2019. Two-dimensional discrete element simulation of the mechanical behavior and strain localization of anisotropic dense sands. *Granular Matter* **21**, 1–16.

Midi, G.D.R. 2004. On dense granular flows. *European Physical Journal E* **14**, 341–365.

Mohammad, S., Ehsan, B., Feizabad, E., Rahmani, R. 2018. Discrete Element Modeling of Drained Triaxial Test: Flexible and Rigid Lateral Boundaries. *International Journal of Civil Engineering* **16***,* 1463–1474.

Negi, M., Mukherjee, M. 2022. Assessment of macro and micro level heterogeneities for characterizing mechanical behavior of sand in biaxial test employing DEM, in: Proc. 15th World Congress on Computational Mechanics and 8th Asian Pacific Congress on Computational Mechanics WCCM-APCOM. Yokohama, Japan.

Tian, J., Liu, E. 2018. Effect of particle shape on micro- and mesostructure evolution of granular assemblies under biaxial loading conditions. *Comptes Rendus - Mecanique* **346**, 1233–1252.

Tian, J., Liu, E., He, C. 2020. Shear band analysis of granular materials considering effects of particle shape. *Acta Mechanica* **231**, 4445–4461.

Wang, Y.H., Leung, S.C., 2008. A particulate-scale investigation of cemented sand behavior. *Canadian Geotechnical Journal* **45**, 29–44.

Widuliński, L., Tejchman, J., Kozicki, J., Leśniewska, D. 2011. Discrete simulations of shear zone patterning in sand in earth pressure problems of a retaining wall. *International Journal of Solids and Structures* **48**, 1191–1209.